RESEARCH ARTICLE

Key Points:
- Laboratory spectra and scattering models confirm the presence of chloride salt deposits on Mars
- THEMIS spectra of salt deposits are consistent with the presence of approximately 10–25 wt % halite
- Salts were deposited in either a lacustrine/playa setting or by late-stage groundwater upwelling

Correspondence to:
T. D. Glotch,
timothy.glotch@stonybrook.edu

Constraints on the composition and particle size of chloride salt-bearing deposits on Mars

Timothy D. Glotch[1], Joshua L. Bandfield[2], Michael J. Wolff[2], Jessica A. Arnold[3], and Congcong Che[1]

[1]Department of Geological Sciences, Stony Brook University, Stony Brook, New York, USA, [2]Space Science Institute, Boulder, Colorado, USA, [3]Department of Physics, University of Oxford, Oxford, UK

Abstract Chloride salt-bearing deposits on Mars were discovered using the Mars Odyssey Thermal Emission Imaging System (THEMIS) and have been characterized by both mid-infrared (MIR) and visible-to-near-infrared (VNIR) remote sensing instruments. The chloride salt-bearing deposits exhibit a blue slope at MIR wavelengths and a featureless red slope at VNIR wavelengths. These deposits also lack strong 3 μm bands in VNIR spectra, indicating that they are desiccated compared to the surrounding regolith. The lack of VNIR spectral features suggests that an anhydrous chloride salt, the most likely of which is halite, is responsible for the observed spectral slope. In this work, we use laboratory spectra and a hybrid T-matrix/Hapke light scattering model to constrain the particle sizes and salt abundances of the Martian chloride salt-bearing deposits. Our work shows that the two broad spectral classes of these deposits observed by THEMIS can be explained by a difference in the particle size of the admixed silicate regolith. In all cases, chloride salt abundances of 10–25% are required to match the THEMIS data. The chloride salt abundances determined in this work suggest deposition in a lacustrine/playa setting or in association with late-stage groundwater upwelling.

1. Introduction

Chloride salts have been identified on Mars using the Mars Odyssey Thermal Emission Imaging System (THEMIS) and Mars Reconnaissance Orbiter Compact Reconnaissance Imaging Spectrometer for Mars (CRISM) [*Osterloo et al.,* 2008, 2010; *Murchie et al.,* 2009; *Wray et al.,* 2009; *Glotch et al.,* 2010; *Ruesch et al.,* 2012]. They are identified in mid-infrared (MIR) Thermal Emission Spectrometer (TES) and THEMIS data by the presence of a distinctive blue slope, resulting in a steady decrease in apparent emissivity with increasing wavelength (decreasing wave number) over the 8–12 μm spectral range. At visible/near-infrared (VNIR) wavelengths, these same deposits show a featureless red slope relative to the surrounding terrain over the ~1–2.6 μm range in CRISM reflectance data. A positive 3 μm feature in CRISM and Observatoire pour la Minéralogie, l'Eau, les Glaces et l'Activité (OMEGA) ratio reflectance spectra supports the interpretation that the deposits are desiccated compared to the surrounding terrains [*Murchie et al.,* 2009; *Glotch et al.,* 2010; *Ruesch et al.,* 2012]. The apparent desiccation of these terrains is supported by evidence for desiccation cracks in high-resolution imagery [*El-Maarry et al.,* 2013, 2014].

The interpretation of these deposits as chloride salt-bearing has been somewhat controversial due to the lack of diagnostic spectral absorptions of anhydrous chlorides in both the VNIR and MIR spectral ranges. Despite this, these materials have unusual spectral properties that are quite distinct from most other materials present on planetary surfaces. For example, the distinctive blue slope of chloride deposits in MIR spectra is due to the low emissivity of chloride salts. Laboratory data also show that the characteristic CRISM spectra for these regions can be matched by mixtures of anhydrous chloride salts and silicates [*Jensen and Glotch,* 2011; *Ruesch et al.,* 2012].

Here we report on a new spectral class of chloride salt-bearing deposits found on Mars and, for the first time, constrain the abundances and particle sizes of salts and silicates present in these deposits. The new class of deposits exhibits the same distinct blue slope in THEMIS data, but their characteristic spectra display a unique concave down spectral shape.

For this work, we acquired MIR emissivity spectra of the suite of silicate/halite mixtures described by *Jensen and Glotch* [2011]. We use these data, supported by a hybrid light scattering model based on the multiple sphere T-matrix (MSTM) model [*Mackowski and Mishchenko,* 2011] and Hapke's thermal emissivity model [*Hapke,* 1996], to constrain the salt content and silicate particle size of chloride salt-bearing deposits on Mars.

Table 1. Image IDs and Ancillary Information for the 10 THEMIS Images Analyzed for This Study

Image ID	Center Longitude	Center Latitude	Minimum Temperature (K)	Maximum Temperature (K)
I33927002	178.01	-34.35	249.30	299.78
I35565002	91.50	-18.72	214.55	277.78
I36355001	343.74	-11.74	198.17	266.35
I39307007	113.79	-2.27	217.99	278.39
I39643002	166.80	-18.32	221.56	276.10
I40123002	357.46	-31.98	234.72	287.03
I41186002	291.00	-34.94	262.06	304.67
I41227002	190.68	-21.55	246.90	302.04
I41850005	216.33	-33.30	263.02	307.38
I42789003	129.24	-30.47	243.39	287.37

Chloride salt-bearing deposits on Mars occur in a variety of geologic contexts, including possible paleolakes, crater fill, inverted channels, and distributary fans [*Osterloo et al.,* 2008, 2010; *Murchie et al.,* 2009; *Wray et al.,* 2009; *Glotch et al.,* 2010; *Ruesch et al.,* 2012; *El-Maarry et al.,* 2013; *Hynek et al.,* 2015; *Osterloo and Hynek,* 2015]. These studies generally support an interpretation that the deposits formed in an aqueous environment. Considering these data in tandem with the data presented here and in *Jensen and Glotch* [2011], who showed that the near-IR spectral character of the deposits is consistent with halite/silicate mixtures, we conclude that anhydrous chloride salt, specifically halite, is the only mineral that is both geologically plausible and matches the observed spectral properties (transparent with a low emissivity over the required wavelength ranges).

2. Data and Methods

2.1. THEMIS Data Analysis

Osterloo et al. [2010] identified 641 individual chloride salt deposits covered by several hundred high-quality THEMIS daytime images. While an exhaustive spectral survey of each of the sites identified by *Osterloo et al.* [2010] is impractical, we used the Java Mission-planning and Analysis for Remote Sensing (JMARS) software [*Christensen et al.,* 2009] to examine 10 occurrences of the chloride salt deposits in high-quality THEMIS images, based on maximum surface temperature, for detailed spectral analysis. THEMIS images were atmospherically corrected using the methods of *Bandfield et al.* [2004a]. These images, the associated center latitudes and longitudes of the chloride salt units and minimum and maximum surface temperatures, are listed in Table 1. To summarize briefly, we (1) applied a correction to remove a constant radiance contribution due to atmospheric emission, (2) retrieved surface emissivity using low spatial resolution, but high spectral resolution TES data covering the region of interest, (3) mapped the derived surface emissivity to THEMIS data to derive the atmospheric attenuation of surface emitted radiance, and (4) corrected for this atmospheric component to derive surface emissivity for the entire image.

2.2. Sample Selection and Preparation

Our samples consist of physical mixtures of halite and flood basalt. The basalt was purchased from Ward's Science and is from the Columbia River Plateau. The halite was acquired from Acros Organics (reagent grade 99% + synthetic NaCl). The flood basalt and halite samples were crushed with a steel mortar and pestle and dry sieved to produce a range of coarse size fractions. To produce a <10 μm size fraction, samples were separated in ethanol using Stokes' settling method [*Day,* 1965; *Gee and Bauder,* 1986; *Salemi et al.,* 2010]. Subsequent to settling, samples were dried at 80°C. For this work, we use four size fractions from *Jensen and Glotch* [2011]: 250–355, 125–180, 63–90, and < 10 μm. The samples and preparation methods are described in detail by *Jensen and Glotch* [2011]. Samples are currently stored in the Stony Brook University Vibrational Spectroscopy Laboratory and are available upon request.

2.3. Laboratory Spectroscopic Measurements

We heated each sample to 80°C overnight prior to spectral measurements. We collected emissivity spectra of each sample over the 2000–200 cm^{-1} (5–50 μm) spectral range using a Nicolet 6700 Fourier transform infrared (FTIR) spectrometer modified to measure sample emitted radiance. Each spectrum is an average of 256 scans and was calibrated using a blackbody target heated to 70°C and 100°C in the manner of *Ruff* et al. [1997].

Note that our laboratory spectra are converted to emissivity in a slightly different manner than the remotely sensed emissivity spectra of the Martian surface from TES. TES spectra are converted to emissivity by dividing radiance spectra by a blackbody of the highest brightness temperature determined within a $50\,cm^{-1}$ band near $1300\,cm^{-1}$ [*Bandfield et al.*, 2000]. Our laboratory emissivity spectra were calculated in a similar manner, although the position of the maximum brightness temperature was not constrained. The result is that some of our laboratory spectra do not exhibit the overall slopes and emissivity values > 1.0 seen in TES spectra of Martian chloride salt deposits [e.g., *Osterloo et al.*, 2008, Figure 3b].

2.4. Modeling Emissivty Spectra and NaCl Optical Constants

We utilized the multiple sphere T-matrix (MSTM) model of *Mackowski and Mishchenko* [2011] to exactly calculate the phase function and "near-field" scattering properties of clusters of closely packed mineral grains (halite and silicate). The goals of this modeling effort are to (1) provide a theoretical frame of reference for the laboratory measurements, (2) calculate Mars surface spectra using actual Mars remote sensing data (Mars dust optical constants from *Wolff et al.* [2006]) to provide a more direct comparison between Martian data and laboratory analyses, and (3) investigate how the increase in abundance of transparent chloride salt alters scattering parameters such as the phase function. The fundamental inputs into this model are the real and imaginary indices of refraction, n and k, of the materials of interest and the position and size parameter ($x = \frac{2\pi}{r}$ where r is the radius of the particle) of each sphere in the cluster. For each sphere in the cluster, the incident and scattered fields can be represented by regular and outgoing vector spherical wave function expansions, centered about the origin of the sphere. The sum of the scattered fields for each sphere represents the scattered field of the cluster as a whole. The mathematical formulation and details of code implementation are given by *Mackowski and Mishchenko* [1996, 2011].

We calculate hemispherical emissivity according to equation (64) of *Hapke* [1996], which approximates the emissivity of a surface heated from below and is appropriate for comparison to our laboratory measurements:

$$\epsilon_h = 2\gamma/(\zeta + \gamma), \tag{1}$$

where

$$\gamma = \sqrt{1-w}, \tag{2}$$

$$\text{and } \zeta = \sqrt{1 - \beta \cdot w}. \tag{3}$$

Here β is the hemispherical asymmetry parameter, γ is the thermal albedo factor, and ζ is the thermal asymmetry factor. The MSTM code calculates the asymmetry parameter of the cluster phase function, g, according to

$$g = 1/2 \int d(\cos\theta) p(\theta) \cos(\theta) = \langle \cos(\theta) \rangle = u, \tag{4}$$

where θ is scattering angle and $p(\theta)$ is the single-scatting particle phase function [*Mishchenko*, 1994]. Using the Sagan-Pollack approximation [*Sagan and Pollack*, 1967; *Wiscombe and Grams*, 1976], $\beta \approx g$, we replace β in equation (3) with g, which is derived from the MSTM calculation.

The MSTM code also calculates the scattering efficiency, Q_{sca}, and total extinction, Q_{ext}, providing additional input parameters for our spectral analysis. At each wavelength, we calculate the single-scattering albedo according to

$$w = Q_{sca}/Q_{ext}. \tag{5}$$

To model finely particulate chloride salt-bearing deposits on Mars, we used a sphere cluster consisting of 377 randomly close-packed (packing fraction of ~0.6) 10 μm diameter spheres generated using a molecular dynamics-based Fortran code described in *Donev et al.* [2005] and available at http://cims.nyu.edu/~donev/ Packing/PackLSD/Instructions.html. The number of particles in the cluster represents a compromise between achieving a large enough number of particles to reasonably model a regolith surface and the computational cost of the calculations, which increases as the cube of the cluster size parameter. Each sphere in the cluster was assigned either the optical constants of Mars dust (derived by *Wolff et al.* [2006]) or halite (derived specifically for this work), and the model was run at roughly $20\,cm^{-1}$ intervals
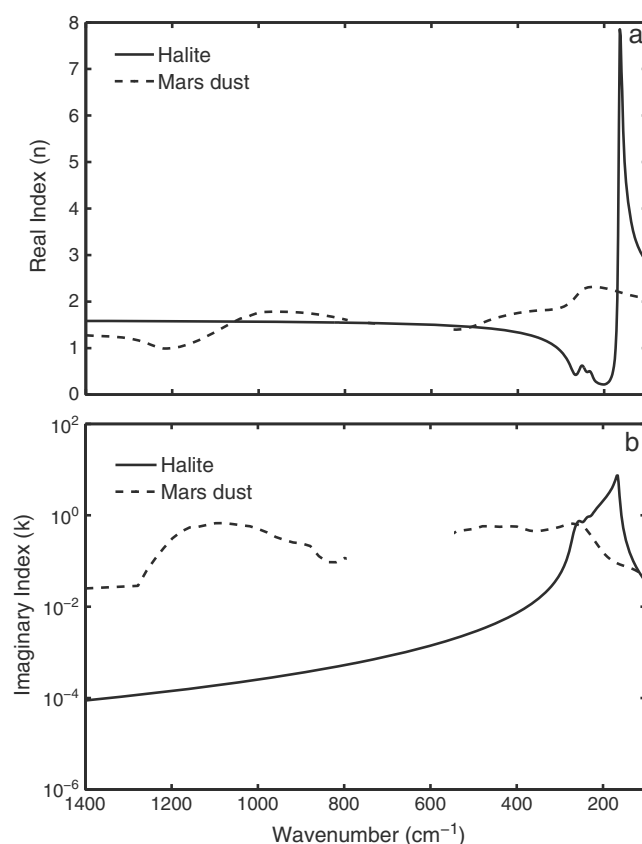
Figure 1. Refractive indices of Mars dust [*Wolff et al.,* 2006] and halite (generated in this work) used in our scattering model. (a) Real index of refraction. (b) Imaginary index of refraction.
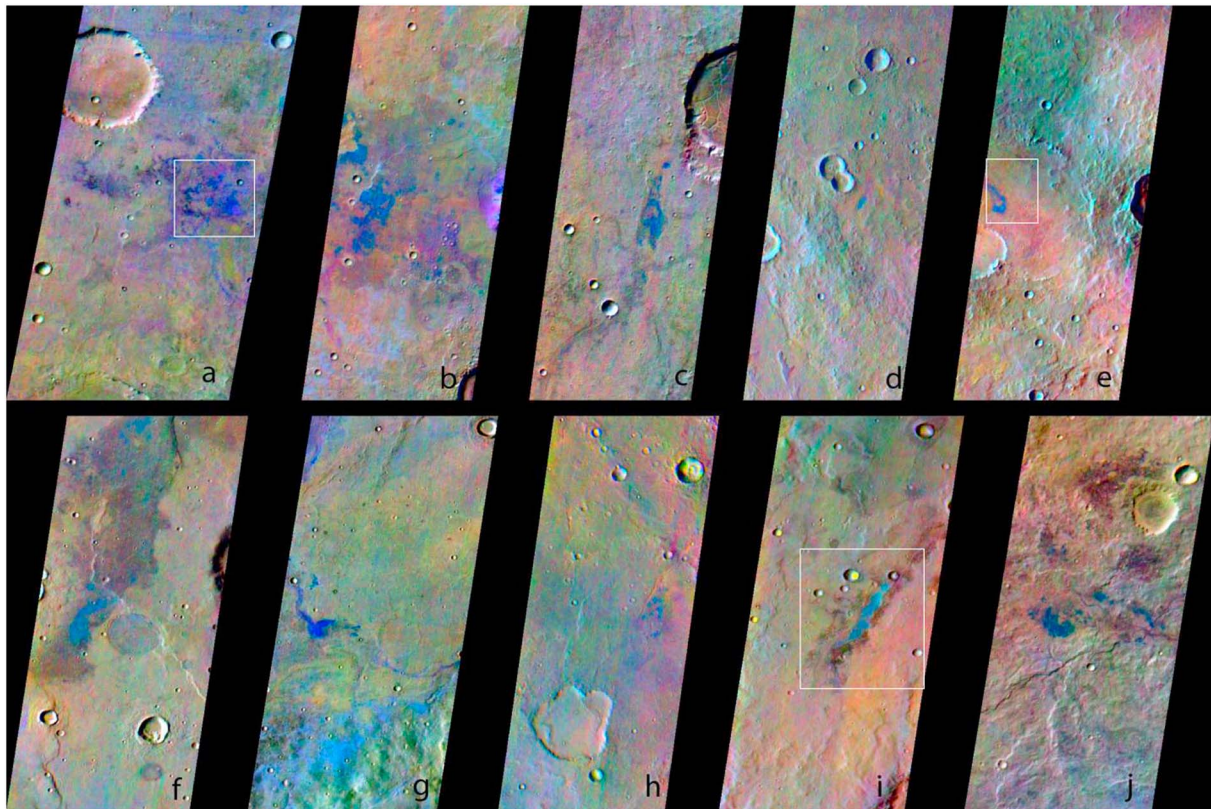
between 400 and 1538 cm^{-1} to build the spectra. We varied the percentage of halite in the model between 0 and 95% to assess the effects of halite abundance on the resulting calculated mid-IR spectra.

To model the halite refractive indices, we used the Stony Brook University Vibrational Spectroscopy Laboratory's Nicolet 6700 FTIR spectrometer to acquire a specular reflectance spectrum of a pressed pellet of reagent-grade halite. The mid-IR spectrum (2000–400 cm^{-1}) was acquired using a deuterated L-alanine doped triglycine sulfate (DLaTGS) detector with a KBr window. A far-IR spectrum (600–100 cm^{-1}) was acquired using a DLaTGS detector with a polyethylene window. The far-IR spectrum was scaled down by ~3% to account for slight differences in detector linearity over the overlapping wavelength range and merged with the mid-IR spectrum at ~500 cm^{-1}. The mid-IR spectrum was an average of 256 scans. Due to a lower signal-to-noise ratio for the far-IR detector, we averaged 1024 scans to construct the far-IR spectrum. We then used Lorentz-Lorenz dispersion theory [*Spitzer and Kleinman,* 1961] to determine the real and imaginary refractive indices of halite from the merged spectrum. Details of the model can be found in *Glotch et al.* [2007] and *Glotch and Rossman* [2009]. Halite optical constants and dispersion parameters are shown in Figure 1 and Table 2, respectively, and are archived at http://aram.ess.sunysb.edu/optical_constants.html.

3. Results

3.1. THEMIS Data

For each of the 10 chloride salt locations chosen for this study, we confirmed the detections of *Osterloo et al.* [2010] by creating decorrelation-stretched (DCS) images [e.g., *Gillespie et al.,* 1986] utilizing THEMIS bands 8, 7, and 5 as red, green, and blue (Figure 2). With this band combination, chloride salts typically appear bright blue or bluish-green in the THEMIS DCS images [*Osterloo et al.,* 2008, 2010; *Glotch et al.,* 2010]. The chloride salt sites identified in this study generally consist of rough, irregular, visibly light toned patches on 1–10 km scales, superposing the plains on which they were deposited, often, though not always, in local topographic lows. In two cases (Figures 2g and 2i), the chloride salt deposits are associated with inverted channel topography features, suggesting as association with at least some flowing surface water.

At decameter spatial scales, substantial geomorphologic differences between the deposits are observed. For example, Figure 3a shows an irregular distribution of salty patches over the local heavily cratered terrain. In this instance, chloride salt deposits appear to cover both local

Table 2. Dispersion Parameters for Halite[a]

| ν (cm^{-1})	γ	$4\pi\rho$
165	0.0361	3.3793
212	0.1869	0.0440
233	0.0767	0.0396
254	0.0825	0.0362

[a]ε_0 = 2.5576.

Figure 2. THEMIS DCS images showing the 10 chloride salt sites characterized in this study. For each image, bands 8, 7, and 5 are assigned to red, green, and blue, respectively. Locations for each chloride salt unit are given in Table 1. (a) I33927002. (b) I35565002. (c) I36355001. (d) I39307007. (e) I39643002. (f) I40123002. (g) I41186002. (h) I41227002. (i) I41850005. (j) I42789003. White boxes in Figures 2a, 2e, and 2i indicate the positions of Figures 3a–3c. Deposits in Figures 2d, 2e, and 2h occur in moderately dusty regions, resulting in anomalous THEMIS spectra displayed in Figure 4.

topographic highs and lows, and there appears to be little correlation with fluvial features. By contrast, comparatively smaller deposits are shown in Figures 3b and 3c where chloride salt deposits occur in local topographic lows. In Figure 3b, the chloride salt deposit has been reworked into aeolian bed forms. No such bed forms are obvious in the deposit shown in Figure 3c. However, this deposit (also shown in Figure 2i) is
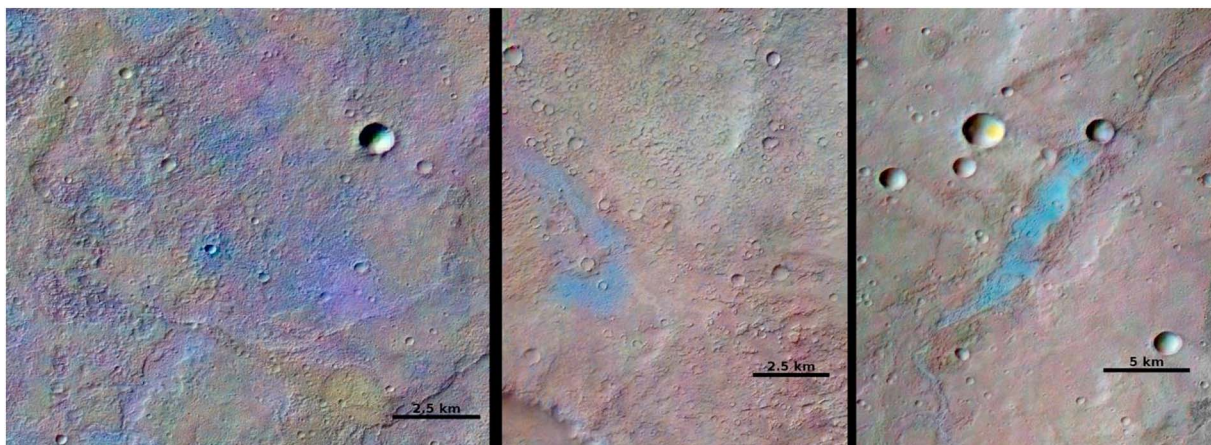
Figure 3. THEMIS DCS images overlaid on Context Camera (CTX) imagery. Blue colors indicate the presence of chloride salt. Salts typically occur in local topographic lows and are associated with rough, high-albedo patches. (a) THEMIS image I33927002 overlaid on CTX image D17_033885_1453_XN_34S182W. (b) THEMIS image I39643002 overlaid on CTX image B18_016585_1635_XN_16S193W. (c) THEMIS image I41850005 overlaid on CTX image P12_005625_1470_XI_33S143W. The deposit in Figure 3b occurs in a moderately dusty region, resulting in one of the anomalous spectra shown in Figure 4.
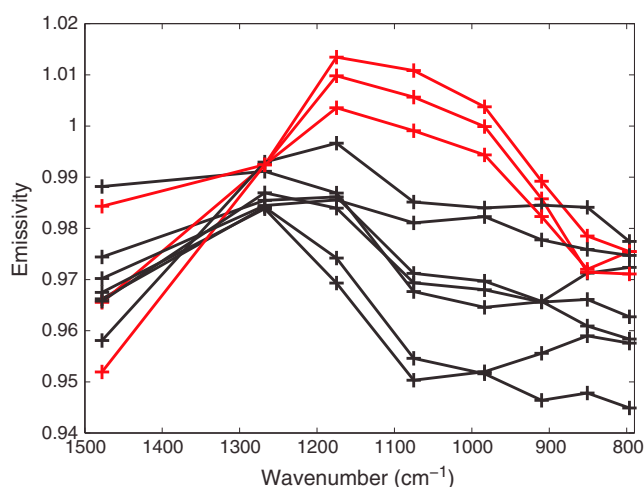
Figure 4. Average atmospherically corrected THEMIS surface emissivity spectra of chloride salt-bearing deposits. Typical spectra (black) have a variety of shapes, but all display blue slopes and absorptions between 1200 and 900 cm^{-1}. Spectra from the three anomalous deposits (red) display similar blue slopes but have emissivity maxima between 1200 and 900 cm^{-1}. Typical errors for the spectra displayed range between 0.005 and 0.01 emissivity units.

clearly associated with inverted channel deposits, suggesting water flowing into and out of the local topographic low in which the chloride salt-bearing deposit sits. This in turn suggests that water may have ponded at the surface in this region for a period of time.

Our spectral survey of the 10 chloride salt locations chosen for this study (Figure 4) found a range of spectral shapes; all of which display a blue slope between 800 and 1200 cm^{-1}. Most display superposed silicate absorptions centered between 1000 and 1100 cm^{-1} that are consistent with the spectral shapes of the local basaltic regolith. However, at three locations (Figures 2d, 2e, and 2h), which have low to moderate dust cover index (DCI) values (Figure 5), we found that the average THEMIS spectra display a blue slope, but with high overall emissivity and a concave down

spectral shape between 900 and 1200 cm^{-1}. Each of these three surfaces has an emissivity maximum in band 4 (1175 cm^{-1} and 8.51 μm) and a steeply dipping emissivity toward higher wave numbers/shorter wavelengths, consistent with multiple scattering by fine particulates. Some spectra have maximum emissivities greater than unity as a result of an atmospheric correction artifact. In all cases, surface emissivity is chosen to be unity in the band of highest brightness temperature. This typically occurs in band 3 or occasionally 9 (bands 1 and 2 are excluded) because the atmospheric dust is most transparent in these bands. If bands 4 or 5 have a higher apparent surface emissivity, the dust more than compensates for that, and those bands still appear with lower brightness temperatures in the uncorrected spectra.
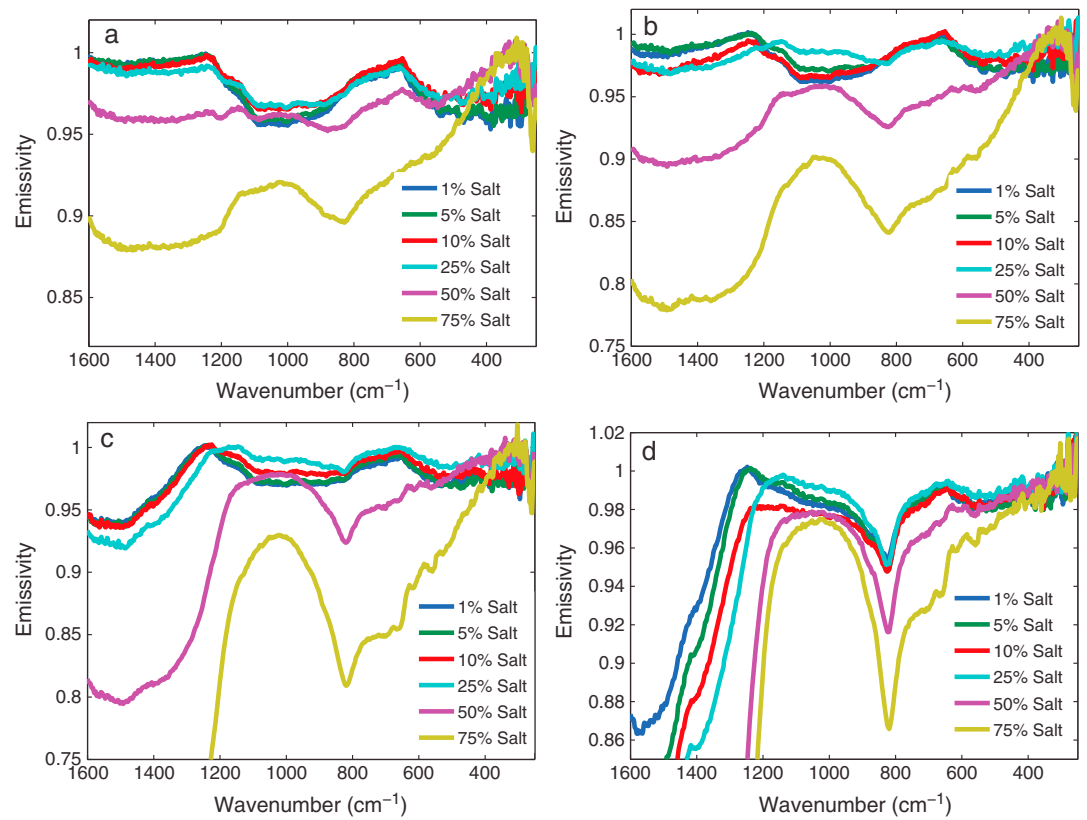
3.2. Laboratory Spectra

Spectra of the particulate mixtures are shown in Figure 6. The 250–355 μm size fraction with 1–10% halite (Figure 6a) displays emissivity spectra typical for basalt. Spectra of these samples have broad absorptions from ~1200–600 cm^{-1} and ~700–300 cm^{-1}, similar to the TES Surface Type 1 (ST1) [*Bandfield et al.,* 2000] or Group 3 spectrum [*Rogers and Christensen,* 2007]. The 1 and 5% halite spectra are nearly identical, with emissivity maxima of unity at 1252 cm^{-1} and comparable spectral contrast. At 10% halite content, the overall
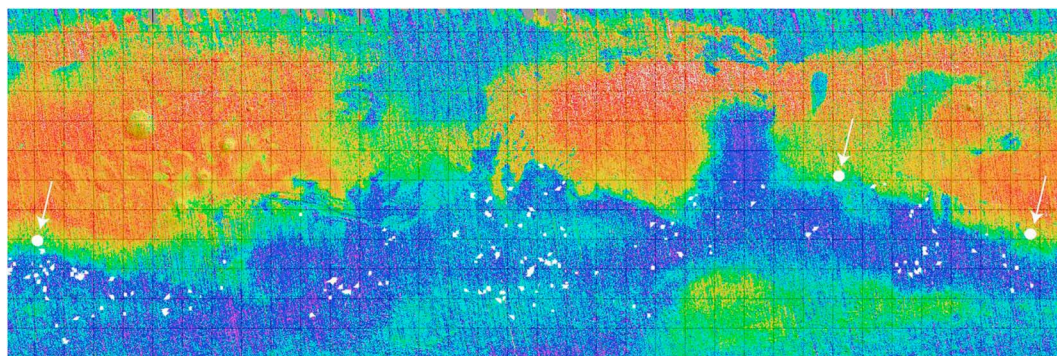
Figure 5. *Osterloo et al.* [2010] chloride salt occurrence database (white polygons) overlaid on TES dust cover index (DCI) [*Ruff and Christensen,* 2002]. The DCI is displayed from values of 0.92 (red) to 1.00 (purple). Three sites in moderate dust cover (circles marked by white arrows) display anomalous spectral character in THEMIS data. DCI values for the three chloride salt deposits are 0.959 (image I39643002), 0.964 (image I39307007), and 0.947 (image I41227002).

Figure 6. Laboratory emissivity spectra of basalt-halite mixture powders. (a) 250–355 μm size fraction. (b) 125–180 μm size fraction. (c) 63–90 μm size fraction. (d) < 10 μm size fraction.

spectral contrast is reduced slightly, and the emissivity maximum in the Christiansen feature (CF) region shifts to $1245\,cm^{-1}$, with an emissivity of 0.995. At 25% halite content, the spectral contrast is further reduced, and the emissivity maximum shifts to $1240\,cm^{-1}$ with a maximum emissivity in the CF region of 0.99. For both the 10 and 25% halite spectra, the laboratory calibration code determined that the maximum brightness temperatures (where emissivity is taken to be unity) occurs at $\sim 1640\,cm^{-1}$, far from the typical CF region for silicates. The spectra drastically change for the 50% and 75% halite spectra, which have broad emissivity maxima between ~ 1200 and $600\,cm^{-1}$, where the other spectra have absorptions. Over the $1600–600\,cm^{-1}$ range, the maximum emissivity for the 50% halite spectrum is 0.98, while for the 75% halite spectrum, it is 0.94. The emissivity maxima for these spectra occur at $313\,cm^{-1}$.

The trends seen in the 125–180 μm size fraction spectra (Figure 6b) are similar to those seen in the 250–355 μm size fraction, although more pronounced. Again, the 1% and 5% halite spectra are very similar, with identical emissivity maxima of unity at $1243\,cm^{-1}$. The 5% halite spectrum has a slightly reduced spectral contrast, with a minimum emissivity between 1200 and $600\,cm^{-1}$ of 0.97, compared to a value of 0.96 for the 1% emissivity spectrum. At 10% halite, the maximum emissivity in the CF region is reduced to 0.995, while the absolute maximum emissivity is unity at $651\,cm^{-1}$. At 25% halite, the spectral contrast shallows considerably, and the emissivity maximum in the CF region shifts from $1243\,cm^{-1}$ to $1148\,cm^{-1}$, with a maximum value of 0.994. The broad emissivity minimum present for the lower halite contents is nearly gone, replaced by an inverted Reststrahlen band between $\sim 1150\,cm^{-1}$ and $820\,cm^{-1}$. The 50% halite spectrum has a broad, concave down feature between $\sim 1300\,cm^{-1}$ and $820\,cm^{-1}$, with a maximum emissivity of 0.96. The 75% halite spectrum is similar, with a maximum emissivity of only 0.90 in the same spectral range. The absolute maximum emissivities for each of the 25%, 50%, and 75% halite spectra occur at $\sim 313\,cm^{-1}$, with values of unity.

At a size fraction of 63–90 μm (Figure 6c), differences from the coarser size fractions are apparent. For halite contents less than 10%, the spectra are comparable, with each having an emissivity maximum of unity at $1243\,cm^{-1}$ and with a reduction in spectral contrast with increasing halite content. The 10% halite spectrum
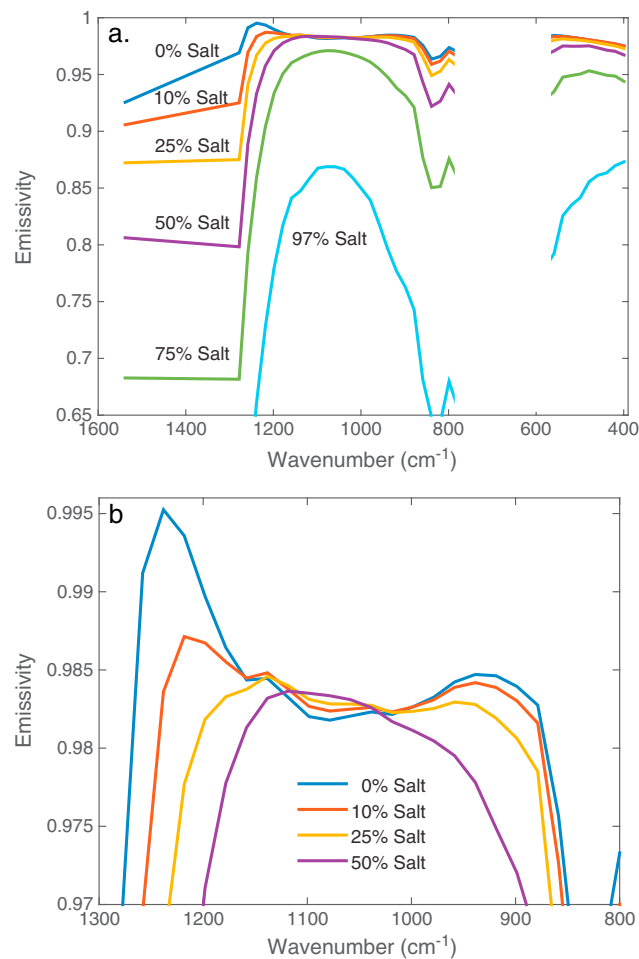
Figure 7. Modeled spectra of Mars dust/halite mixtures. (a) Full spectra covering the 399–1538 cm^{-1} (6.5–25 μm) range with halite contents ranging from 0% to 97%. Increasing halite content leads to an overall reduction in emissivity, a shift of the CF to lower wave numbers (longer wavelengths), and a change in spectral shape in the middle portion of the spectrum from slightly concave up to strongly concave down. (b) Same spectra as in Figure 7a, zoomed into the 800–1300 cm^{-1} region, highlighting the gradual change in spectral shape with increasing halite content.
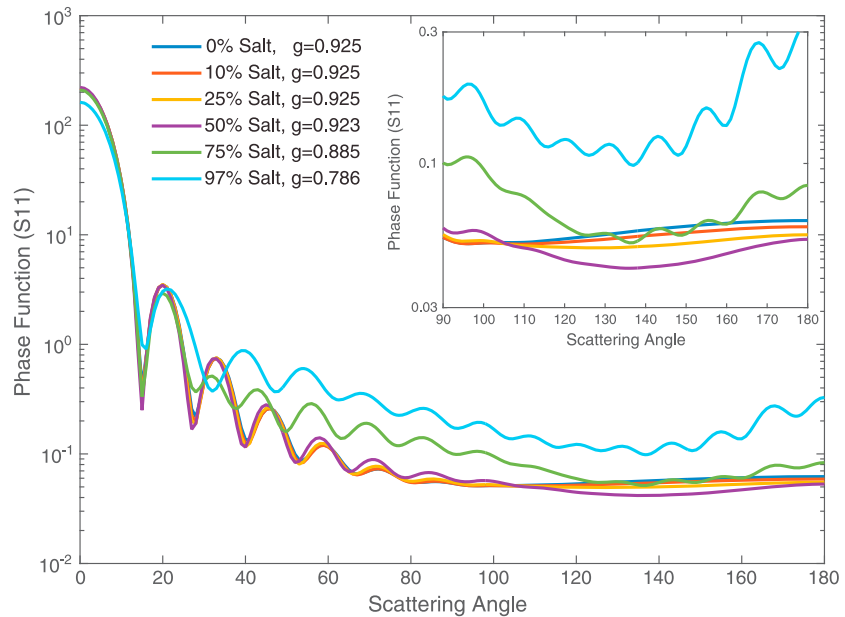
also displays a slight decrease in emissivity between 1243 and 827 cm^{-1}, which is absent at lower halite contents. At 25% halite content, the CF shifts to 1142 cm^{-1}, and the spectrum displays a strong blue slope with low spectral contrast between 1142 and 827 cm^{-1}. The 50 and 75% halite spectra display dramatic differences from the lower halite content spectra, with strongly concave down features between 1300 and 819 cm^{-1} and maximum emissivities of 0.98 and 0.93, respectively.

The < 10 μm size fraction (Figure 6d) differs substantially in its spectral behavior compared to all of the coarser size fractions. For halite contents of 1 and 5%, the spectra have CF positions of 1256 and 1243 cm^{-1}, respectively, and display a blue slopes with low spectral contrast, between the CF position and 820 cm^{-1}. The 10% halite spectrum shows the same general behavior, but with a CF position of 1237 cm^{-1} and a maximum emissivity in the CF region of 0.98. The 25% halite spectrum displays a CF at 1140 cm^{-1}, with a minimum emissivity of 0.99, and a slight concave down shape between 1300 and 820 cm^{-1} that is more pronounced in the higher halite content spectra. At 50 and 75% halite contents, the spectra display strong concave down spectral shapes between 1300 and 820 cm^{-1}, with maximum emissivities of 0.98 and 0.97, respectively.

3.3. Model Results

Modeled spectra for the cluster of 10 μm halite and Mars dust particles are shown in Figure 7. The pure Mars dust spectrum (0% halite) is consistent with typical TES bright region spectra of Mars, with a CF position of 1238 cm^{-1} and a maximum emissivity of 0.995. The spectrum includes a broad, shallow, concave up spectral feature between 938 and 1238 cm^{-1}, and the prominent silicate transparency feature at 839 cm^{-1} is well modeled. At 10% halite content, the CF is shifted to 1218 cm^{-1}, and the maximum emissivity is reduced to 0.987. The broad central feature is considerably shallowed, although it is still slightly concave up. At 25% halite, the maximum emissivity is reduced to 0.985, and the CF is shifted to 1138 cm^{-1}. The overall shape of the broad central feature is concave down, although there is still a local minimum with a shallow concave up profile centered at 1078 cm^{-1}. The emissivity of the 25% halite spectrum at most wavelengths is slightly lower than the 10% halite spectrum at most wavelengths. At 50% halite content, the region between 1238 and 919 cm^{-1} is strongly concave down, with a maximum emissivity of 0.983 at 1118 cm^{-1}. The emissivity of the spectrum is substantially reduced compared to lower halite contents. Further dramatic changes to the spectra are seen for 75 and 97% halite contents. Both spectra are dominated by a strongly concave down broad feature centered at 1078 cm^{-1}. The maximum emissivities of these spectra are 0.97 and 0.87, respectively.

Figure 8. Scattering phase functions derived from MSTM for the halite/dust clusters modeled in this work. S_{11} denotes that the phase function is the (1,1) element of the Stokes scattering matrix.

Figure 8 shows the scattering phase functions and associated asymmetry parameters at 1018.5 cm^{-1} (9.8 µm) for each of the clusters we modeled in MSTM. This chosen frequency (1018.5 cm^{-1}) is near the center of the broad feature in our laboratory and modeled spectra that originates as a shallow concave up feature and inverts to a strongly concave down feature with increasing halite content (Figures 6 and 7). As with the spectra shown in Figure 7, there is little difference between the scattering phase fun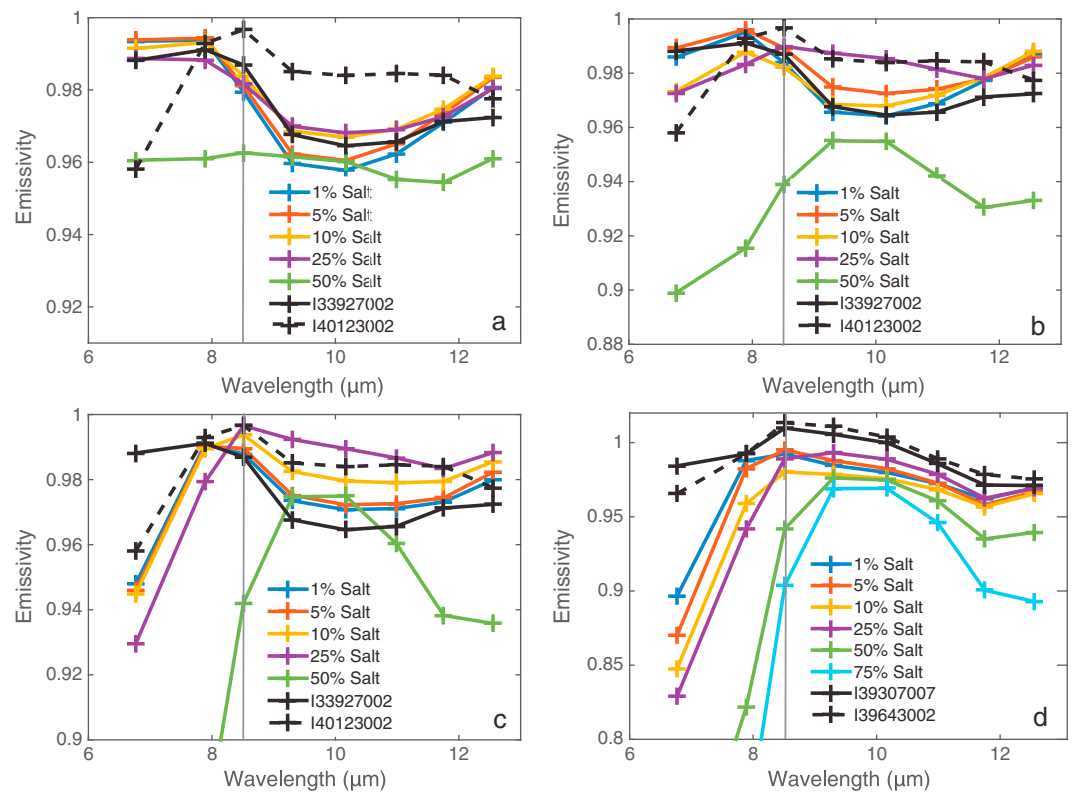ctions and asymmetry parameters for the 0%, 10%, and 25% halite clusters, especially at low-scattering angles. Between ~120 and 180°, the phase function curves separate a bit, with higher halite abundance clusters being slightly less forward scattering (lower asymmetry parameters) than clusters with lower halite abundances. At 50% halite abundance, the phase function starts to divert from the lower halite abundance curves, even at phase angles as low as 30°. At 75% and 97% halite abundances, the phase curves divert substantially from the lower halite contents, with generally higher magnitudes at scattering angles higher than 50°. An exception is that the 75% halite content phase curve has a lower magnitude than the 0 and 10% halite content curves between ~125 and 160°.

Figure 9. Near-field visualization of the electric field magnitude, $|E|^2$, surrounding clusters of Mars dust and halite particles at 1018.5 cm^{-1} (9.8 µm). (a) 10% halite. (b) 25% halite. (c) 50% halite. (d) 97% halite. White arrows indicate spheres with higher internal E field magnitudes than surrounding spheres. As the halite component of the cluster is increased, the clusters become more transparent, resulting in higher electric field magnitudes in the cluster interiors.
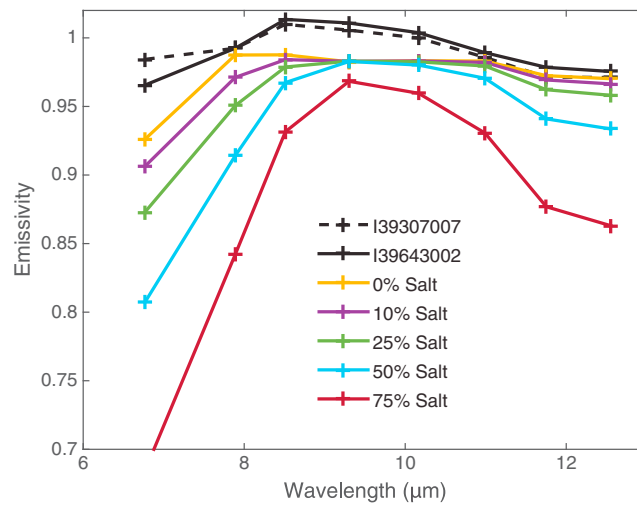
Figure 10. Laboratory spectra of halite/basalt mixtures convolved to THEMIS spectral sampling and compared with representative THEMIS spectra of chloride salt-bearing surfaces on Mars. Vertical lines indicate the position of THEMIS band 4. (a) 250–355 µm size fraction. (b) 125–180 µm size fraction. (c) 63–90 µm size fraction. (d) <10 µm size fraction. THEMIS spectra taken from chloride salt deposits in dustier regions of Mars.

We used MSTM to gain additional insight into the effects of increasing transparency and changing phase function due to increased halite content. In our model, we calculate the near-field electric field magnitude relative to the magnitude of the field of the incoming beam, $|E|^2$, surrounding and within our cluster of spheres at 1018.5 cm^{-1} (9.8 µm) for 10, 25, 50, and 97% halite content. The E field magnitude can be thought of as a proxy for scattering, such that high magnitudes within the cluster indicate transparency at the chosen wavelength, while low magnitudes indicate high opacity. The results of these near-field models are shown in Figure 9, which depicts $|E|^2$ in a plane taken through the center of the modeled clusters. At 10 and 25% halite content (Figures 9a and 9b), the electric field magnitude at the center of the cluster is at or close to 0, indicating that the cluster is opaque at this wavelength. At 25% halite, several spheres can be seen with low (~0.17–0.32 V^2/m^2) but nonzero electric field magnitudes (white arrows in Figure 9b), indicating increased transmission of light through the cluster. At 50% halite, the cluster is clearly more transparent, with multiple spheres with nonzero electric field magnitudes toward the center of the cluster (white arrows in Figure 9c). As would be expected, the 97% halite cluster is nearly completely transparent, with the center sphere (white arrow in Figure 9d) in the cluster displaying electric field magnitudes ~1.8 V^2/m^2 and numerous other spheres in the cluster exhibiting high E field magnitudes, indicating their transparency.

4. Discussion

4.1. Comparison of Laboratory and Modeled Spectra to THEMIS

To directly compare our laboratory and modeled spectra to THEMIS data of chloride salt-bearing deposits on Mars, we resampled them to THEMIS spectral sampling using the THEMIS filter functions. Convolved laboratory spectra are shown in Figure 10, and convolved modeled spectra are shown in Figure 11. Emissivity maxima and calculated slopes for the THEMIS data are shown in Figure 4, and the laboratory data convolved to THEMIS spectral sampling are shown in Table 3. The THEMIS data fall into two broad spectral

Figure 11. MSTM/Hapke model spectra of clusters of 10 μm spheres convolved to THEMIS spectral sampling and compared with representative THEMIS spectra of chloride salt-bearing surfaces from moderately dusty regions of Mars. Vertical line indicates the position of THEMIS band 4.

classes (Figure 4) that are strongly controlled by particle size and chloride salt abundance. Laboratory data convolved to THEMIS spectral sampling constrain the particle sizes and chloride salt abundances that give rise to these two spectral classes.

As suggested by the full-resolution laboratory data, the coarsest size fraction (250–355 μm; Figure 10a) mixtures generally do not match representative THEMIS spectra of chloride salt-bearing surfaces at any salt content. At lower halite contents, the spectra do not have the blue slope that is characteristic of the THEMIS data. At the highest halite contents, the overall emissivity is much too low and the magnitude of the inverted silicate feature is much too

Table 3. Emissivity Maximum Positions and Calculated Slopes for the THEMIS Spectra Shown in Figure 4 and the Basalt/Halite Mixture Spectra Resampled to the THEMIS Spectral Bands

THEMIS Image/Sample	Emissivity Maximum (μm)	8.51–12.56 μm Slope ($\times 10^{-3}$)
I33927002	7.89	3.58
I35565002	7.89	7.23
I36355001	8.51	6.86
I39307007	8.51	9.56
I36943002	8.51	9.38
I40123002	8.51	4.74
I41186002	7.89	2.90
I41227002	8.51	6.94
I41850005	8.51	2.68
I42789003	7.89	5.24
250–355 μm, 1% halite	7.89	-0.28
250–355 μm, 5% halite	7.89	-0.58
250–355 μm, 10% halite	7.89	-0.01
250–355 μm, 25% halite	7.89	0.31
250–355 μm, 50% halite	7.89	0.37
250–355 μm, 75% halite	10.17	-0.69
125–180 μm, 1% halite	7.89	-0.81
125–180 μm, 5% halite	7.89	0.84
125–180 μm, 10% halite	7.89	-1.45
125–180 μm, 25% halite	8.51	1.72
125–180 μm, 50% halite	9.30	1.47
125–180 μm, 75% halite	10.17	0.37
63–90 μm, 1% halite	7.89	1.96
63–90 μm, 5% halite	7.89	1.81
63–90 μm, 10% halite	8.51	2.02
63–90 μm, 25% halite	8.51	2.03
63–90 μm, 50% halite	9.30	1.56
63–90 μm, 75% halite	10.17	2.55
<10 μm, 1% halite	8.51	5.66
<10 μm, 5% halite	8.51	6.96
<10 μm, 10% halite	8.51	3.61
<10 μm, 25% halite	9.30	4.90
<10 μm, 50% halite	9.30	5.63
<10 μm, 75% halite	9.30	2.66

large to match the THEMIS data. The trend seen in the 125–180 µm size fraction (Figure 10b) is similar for lower halite contents. Up to 25% halite, the spectra do not have blue slopes. However, at 25% halite, the spectral character changes markedly, as the spectral contrast is greatly reduced, and the spectrum displays a prominent blue slope and low spectral contrast, similar to that seen in some THEMIS data. At 50% halite, the overall emissivity and spectral shape are poor matches to the THEMIS data. For the 63–90 µm size fraction (Figure 10c), the blue slope is present at 10% salt content and becomes more prominent at 25% halite. In both cases, these spectra resemble THEMIS data of the Martian low-albedo chloride salt-bearing sites discussed by *Osterloo et al.* [2008, 2010] and *Glotch et al.* [2010]. As with the coarser size fractions the 50% halite spectrum is a poor match to the THEMIS data. Finally, the finest size fraction (<10 µm) spectra all have concave down spectral shapes and do not match typical THEMIS spectra of chloride salt-bearing surfaces. However, these spectra are broadly similar to THEMIS spectra of chloride salt-bearing surfaces in moderately dusty regions of Mars (Figure 10d). For this size fraction, the range of halite contents (1–25%) providing reasonable matches to the THEMIS spectra is broader, with an emissivity maximum in the same channel. As with the coarser size fractions, high halite contents (50–75%) result in spectra with low emissivities that are not comparable to the THEMIS data and a mismatch in the wavelength where the emissivity maximum occurs.

The modeled spectra of 10 µm spheres (Figure 11) are generally similar to the finest size fraction laboratory spectra and the THEMIS data covering high-albedo chloride salt-bearing deposits, with a key difference. In general, the concave down spectral shape observed in the THEMIS and laboratory data are replicated. However, the spectra are relatively flat rather than sloped through the ~8–11 µm region. As seen in the laboratory data, high halite contents (50–75%) lead to low emissivity spectra that are not consistent with THEMIS data.

The data presented here indicate that both the particle size and the salt content exert a strong influence on spectra of chloride salt-silicate mixtures, even at the relatively coarse spectral resolution of THEMIS. For coarse particulates and low halite contents (<10%), spectra of halite-silicate mixtures have an emissivity maximum at 1268 cm^{-1} (7.89 µm; THEMIS band 3). For all but the coarsest particulates, as halite content increases to 10–25%, the emissivity maximum shifts to 1175 cm^{-1} (8.51 µm; THEMIS band 4). This shift is generally coincident with the appearance of a blue slope in the spectra that is characteristic of chloride salt-bearing surfaces on Mars. As the halite content increases further, to 50–75%, the emissivity maximum shifts further to 1076 cm^{-1} (9.30 µm; THEMIS band 5) or 984 cm^{-1} (10.17 µm; THEMIS band 6), and the spectral emissivity drops substantially. To date, this extreme shift in the emissivity maximum has not been observed on Mars.

4.2. Constraining Chloride Salt Abundance and Particle Size From THEMIS Data

A key parameter that may help constrain the chloride salt content of the deposits is the position of the emissivity maximum in their THEMIS spectra. As seen in Figures 10 and 11, low chloride salt contents (~0–10%) generally result in spectra with an emissivity maximum in THEMIS band 3, while higher chloride salt contents (~10–25%) result in spectra with an emissivity maximum in THEMIS band 4. Laboratory and model data, however, show that the position of the emissivity maximum is also influenced by particle size, with the coarsest particulates maintaining a band 3 emissivity maximum, even for large salt contents. Fortunately, THEMIS data can be used to assess particle size, both qualitatively and quantitatively. The slope between THEMIS bands 1/2 at 6.77 µm and band 3 at 7.89 µm can be used to characterize the "silicate roll-off" in spectra caused by multiple scatterings due to fine particulates at short wavelengths. In general, fine particulates exhibit a steep roll-off in emissivity at wavelengths short of the Christiansen feature, while coarser particulates exhibit a shallow roll-off or lack one entirely. In Figure 4, the black spectra, typical of chloride salt deposits in less dusty regions of Mars, exhibit relatively shallow slopes between bands 1/2 and band 3, suggesting minimal multiple scattering. By contrast, the red spectra, acquired from chloride salt deposits found in duster terrains on Mars, exhibit steeper slopes, suggesting that the band 4 emissivity maxima in spectra of these deposits are at least partially due to the presence of fine particulates.

The spectra of the high-albedo chloride-bearing units are also similar to spectra of optically thin dust coatings on surfaces that occur when the dust is colder than the atmosphere [*Ruff et al.*, 2006; *Hamilton and Ruff*, 2012; *Rivera-Hernandez et al.*, 2015]. Both surfaces can have a characteristic convex down shape of the ~8–12 µm silicate Restrahlen absorption due primarily to scattering (for chlorides) or emission (for dust coatings). In contrast to the chlorides, the convex downward spectral shape due to dust coatings can be caused by a strong temperature contrast between the dust and the substrate. There is little evidence for the presence

of these effects, especially of this magnitude in the THEMIS data. Adjacent surfaces with similar surface temperatures and thermophysical properties as the chloride unit have the spectral properties of surface dust without the unique convex down spectral shape. Despite this, there remains the possibility that the spectral features are due to dust coating effects rather than the presence of chlorides. However, given the uniqueness of the spectral features combined with the ubiquity of dusty surfaces on Mars with similar thermophysical properties, we believe this to be unlikely.

Thermal inertia can be derived from THEMIS data [*Fergason et al.,* 2006; *Christensen and Fergason*, 2013] to help constrain whether the emissivity maximum position of a spectrum is influenced more by particle size or chloride salt content. For instance, the THEMIS spectrum of the chloride salt-bearing deposit from image I33927002 (Figures 2a and 10) has a blue slope but an emissivity maximum in band 3, implying a chloride salt content below ~10%. The thermal inertia of this deposit is $301.1 \pm 16.1\,\mathrm{Jm^{-2}K^{-1}s^{-\frac{1}{2}}}$, corresponding to an effective particle size of ~730 μm [*Presley and Christensen*, 1997], which is coarse sand. By contrast, the THEMIS spectrum from I40123002 (Figures 2f and 10) has both reduced spectral contrast and emissivity maximum at band 4, which is consistent with a higher chloride salt content (up to 25%). The thermal inertia of this deposit is $309.9 \pm 33.2\,\mathrm{Jm^{-2}K^{-1}s^{-\frac{1}{2}}}$, corresponding to an effective particle size of ~824 μm, which is also coarse sand and only slightly different from the previous deposit. No difference between the spectra of these deposits is expected due to the particle size difference, as both particle sizes are much larger than the wavelength of light used to investigate the surfaces. In this case, the thermal inertias of the two deposits strongly suggest that the differences between their spectral properties are caused by chloride salt abundance rather than particle size. It should be noted that the thermal inertias of the chloride salt deposits examined in this study and that of *Osterloo et al.* [2010] generally suggest a coarser particle size than the laboratory spectra we present here. While thermal inertia is often taken as a proxy for the effective particle size of the surface, it can also indicate induration. Thermal inertia is sensitive to the physical properties of the top few centimeters of the surface [*Putzig and Mellon*, 2007], while thermal infrared spectroscopic measurements are only sensitive to the properties of the top ~100 μm. We suggest that the discrepancy between the measured thermal inertias and the laboratory spectroscopic measurements can be explained by chloride salt deposits that are well indurated but friable, resulting in a more finely particulate surface layer. Such a situation could explain both the thermophysical characteristics and the spectral measurements.

Clearly, particle size exerts a strong control on the spectra of chloride salt-silicate mixtures. For the coarsest particulates (greater than hundreds of microns), spectral changes are not apparent, even up to 25% chloride salt content. For these mixtures, surface scattering is the dominant process, and the transparency of the chloride salt does not result in any additional volume scattering. As particle size is reduced, multiple scatterings become more evident, and the transparent chloride salt results in multiply scattered radiation far from the surface to contribute to the overall signal (Figure 9). This effect is most evident for the finest particulates, which show a concave down spectrum with a spectral shape similar to a transmission spectrum. Model results (Figures 7–9) confirm the hypothesis that increased chloride salt content results in increased multiple scatterings from the interior of the cluster. The addition of chloride salt to the cluster also increases the single-scattering albedo at every wavelength. This effect, combined with the lower asymmetry parameters associated with higher chloride salt contents (Figure 8), results in drastic changes to the shapes and lower overall emissivities of the resulting spectra.

The new class of chloride salt-bearing deposits shown here (Figure 4) is spectrally dissimilar to the THEMIS spectra of chloride salt-bearing deposits shown in previous works [*Osterloo et al.,* 2008, 2010; *Glotch et al.,* 2010]. This work shows, though, that the best explanation for this spectral behavior is that these deposits are composed of finely particulate silicates ($<$ ~10 μm) intimately mixed with a low emissivity, transparent material such as anhydrous chloride salt. Therefore, the primary difference between this new class of deposits and those shown in previous works is that the silicate component of these deposits is composed of substantially finer particulates. This is consistent with their locations in dustier regions of Mars and the thermal inertias of these deposits as determined by TES (298, 278, and $201\,\mathrm{Jm^{-2}K^{-1}s^{-\frac{1}{2}}}$ for images I39307007, I36943002, and I41227002, respectively.

4.3. Composition and Origin of Chloride Salt-Bearing Deposits on Mars

The laboratory and modeling work presented here all use halite (NaCl) for the salt fraction in mixtures. We suggest that this is the most likely composition for the chloride salt-bearing deposits on Mars. Previous work

has shown that these deposits are desiccated compared to the surrounding terrain based on the presence of an inverted 3 μm band in CRISM ratio reflectance spectra. These observations do not rule out the presence of water in the form of inclusions, which are common in halite. They only constrain the water abundance to be less than that of the surrounding regolith. However, near-infrared spectra of Martian salt-bearing deposits are characterized by a featureless red slope with no observable hydration bands [*Murchie et al.,* 2009; *Glotch et al.,* 2010; *Jensen and Glotch*, 2011; *Ruesch et al.,* 2012].

Felsic or other alkalai-enriched rocks, while present in volumetrically minor abundances on Mars [*Christensen et al.,* 2005; *Bandfield et al.,* 2004b; *Bandfield*, 2006; *Carter and Poulet*, 2013; *Wray et al.,* 2013; *Sautter et al.,* 2015; *Rogers and Nekvasil*, 2015], are not required to provide the necessary Na for chloride salt-bearing regions. Previous studies [*Bandfield et al.,* 2000; *Christensen et al.,* 2000; *Rogers and Christensen*, 2007] have all shown that the southern highlands of Mars (where most of the Martian chloride salt-bearing deposits occur) are composed primarily of basalt with a substantial modeled plagioclase feldspar fraction, ranging from ~25 to 65%. None of these studies lists the exact plagioclase composition used, but an intermediate composition such as labradorite ($Na_{0.4}Ca_{0.6}Al_{1.6}Si_{2.4}O_8$) is reasonable given the spectral similarities between Martian basalts and Deccan Traps flood basalts, which have labradorite as the primary plagioclase phase [e.g., *Bandfield et al.,* 2000; *Christensen et al.,* 2000; *Wright et al.,* 2011].

Na_2O makes up 4.56 wt % of labradorite using its empirical formula. Assuming a basalt composed of ~35 vol % labradorite (similar to TES Group 4 of *Rogers and Christensen* [2007]) and densities of 2.69 and 2.90 g/cm^3 for labradorite and basalt, respectively, we can calculate that the basaltic crust of this composition is 1.48 weight% Na_2O.

Assuming a mixture of 75 vol % basalt and 25 vol % halite, which is consistent with the high end of our spectral models and a halite density of 2.17 g/cm^3, chloride salt-bearing deposits on Mars are ~10.59 wt % Na_2O. This represents an enrichment of Na_2O by only a factor of 7.16. This number, would, of course, go down if the Martian plagioclase composition was more sodic, as has been observed at Gale Crater [*Vaniman et al.,* 2013; *Sautter et al.,* 2015] or the Martian chloride salt deposits had a lower percentage of halite.

Besides the total abundance of Na in the Martian basaltic crust, we must also assess whether Na can be mobilized by weathering processes and be available to precipitate as halite or another phase. *Hecht et al.* [2009] used the Phoenix Wet Chemistry Laboratory to analyze soils at the Phoenix landing site and found that major cations evolved from the soil were Mg^{2+} (3.3 mM) and Na^+ (1.4 mM), with only minor K^+ (0.38 mM) and Ca^{2+} (0.58 mM). Based on these data, Na^+ is one of the most available cations in the Martian soil. This is consistent with the study of *Nesbitt and Wilson* [1992], who showed that despite the effects of differing rock compositions on leach rates, Na^+ is quickly leached and mobilized during weathering of basaltic rocks. Taken in sum, these points all suggest that the abundance and availability of Na should not be a limiting factor in the development of Martian chloride salt deposits.

Sylvite (KCl) is another potential anhydrous chloride phase, but the global mean K abundance in the Martian crust is only 3300 ppm [*Taylor et al.,* 2006] (compared to an abundance of 2.14% in Earth's continental crust) [*Wedepohl*, 1995, and references therein], and substantial concentration of K would need to occur for sylvite to form even as a minor phase in the Martian chloride salt-bearing deposits. While K is mobile and prone to some concentration under relatively neutral pH weathering conditions, we still view sylvite as an unlikely major phase in Martian chloride salt-bearing deposits given the low initial abundances in the crust.

Other chloride salts are also unlikely. Molysite ($FeCl_3$) is highly deliquescent, readily transforming to hydromolysite ($FeCl_3 \cdot 6H_2O$) upon exposure to moisture. Ferrous Fe chloride, rokünite, is also hydrated ($FeCl_2 \cdot 2H_2O$) as are the major Mg- and Ca-bearing chlorides bischofite ($MgCl_2 \cdot 6H_2O$), sinarjite ($CaCl_2 \cdot 2H_2O$), and antarcticite ($CaCl_2 \cdot 6H_2O$). At the chloride salt content levels required by the THEMIS data, the Martian chloride salt-bearing deposits would exhibit strong hydration features at VNIR wavelengths. Anhydrous forms of these salts are not stable precipitates under the range of temperatures and water activities that were likely present during the formation of Martian chloride salt deposits [*Davila et al.,* 2010]. Furthermore, whereas the deliquescence relative humidity for $CaCl_2$, $MgCl_2$, and $FeCl_3$ ranges from 28 to 45%, NaCl does not start to take up water until a relative humidity of ~75% is reached over a wide range of temperatures [*Greenspan*, 1977; *Cohen et al.,* 1987; *Davila et al.,* 2010].

Chlorides are not the only chlorine salts that might be considered. Perchlorates have been identified in several locations on Mars [*Hecht et al.,* 2009; *Kounaves et al.,* 2010; *Cull et al.,* 2010; *Navarro-Gonzalez et al.,* 2010; *Glavin et al.,* 2013; *Ming et al.,* 2013]. Anhydrous perchlorates are spectrally featureless between 350 and 2500 nm, although hydrated perchlorates show strong H_2O bands near 1.4 and 1.9 μm [*Morris et al.,* 2009; *Bishop et al.,* 2014]. In addition, perchlorates display numerous strong spectral features in the mid-IR [*Pejov and Petruševski*, 2002; *Sutter et al.*, 2016]. Concentrations of perchlorates at the >5% level would likely result in VNIR reflectance and mid-IR emissivity spectra that are inconsistent with the CRISM, TES, and THEMIS data sets. Chlorates, similar to perchlorates, have strong hydration bands at VNIR wavelengths and numerous strong spectral features at mid-IR wavelengths that would be detectable in THEMIS or TES data at 10–25% abundances [*Miller and Wilkins*, 1952; *Sutter et al.*, 2016]. Upon consideration of both the geological plausibility and detailed knowledge of the spectral features of the various phases that might contribute to the spectra of the Martian chloride salt-bearing regions, halite is clearly the most likely candidate for the salt fraction of these deposits.

4.4. Implications for the Origin of Chloride Salt-Bearing Deposits on Mars

Our work has shown that the spectral features of both the typical coarsely particulate and the newly described finely particulate chloride salt-bearing Martian deposits are consistent with chloride salt contents at the 10–25 wt % level. Here we discuss possible formation mechanisms of these deposits. Halite often forms as a vapor phase deposit from volcanic outgassing [e.g., *Naughton et al.,* 1974] and can dominate the surface mineralogy in the immediate vicinity of volcanic vents, potentially consistent with our observations. However, we view this as an unlikely scenario for the Martian deposits, as to date, no volcanic features have been identified in association with them [*Osterloo et al.,* 2010]. Furthermore, deposition by hydrothermal brines associated with volcanism, as suggested for Home Plate at Gusev Crater [*Schmidt et al.,* 2008], resulted in chloride enrichment of <2 wt %, which is much too small to explain the chloride salt abundances derived from THEMIS data.

Freezing can concentrate chlorides in brines. Halite, observed in several SNC meteorites, suggests interactions between water and Martian upper crustal rocks and precipitation from cold brines. [*Gooding et al.,* 1991; *Bridges and Grady,* 1999, 2000]. The abundances of halite in these meteorites, however, are small, with halite and other evaporite phases filling veins and interstitial pore spaces. This mechanism likely cannot explain the abundances of halite observed by THEMIS.

Halite, like sulfates discovered at Meridiani Planum and other regions of Mars [*Gendrin et al.,* 2005; *McLennan et al.,* 2005; *Murchie et al.,* 2009], often forms as solute-rich waters or brines evaporate. Halite is expected to precipitate from SO_4-and HCO_3- poor brines derived from weathering of basaltic rocks [*Tosca and McLennan*, 2006]. Evaporative environments on Mars are most likely to resemble hydrologically closed continental brine systems on Earth. These systems display a variety of mineral assemblages, which include chlorides, carbonates, and sulfates. The primary factor controlling the composition of the evaporite mineral assemblage in a closed basin is the lithology of the leached rocks contributing to the dilute fluid [*Eugster and Hardie*, 1978]. *Eugster and Hardie* [1978] defined five fluid types for continental evaporite basins; the evolution of which determines the mineral assemblages within the basin. In each case, carbonates precipitate first, with the subsequent precipitates determined by the chemistry of the remaining fluid. *Tosca and McLennan* [2006] argued that the "chemical divides" (turning points in chemical evolution) for precipitating fluids on Mars must be different than those that occur on Earth. This is because Martian fluids primarily leached mafic and ultramafic crust—a condition that is relatively rare for terrestrial evaporite systems. Therefore, *Tosca and McLennan* [2006] reevaluated chemical divides and brine evolution for Martian systems and defined five brine evolution pathways. Of these, three result in late-stage brines favoring chloride salt precipitation. In each case, the pathway to the formation of these late-stage brines and precipitates includes the precipitation of carbonates (calcite, siderite, and/or magnesite) and sulfates (gypsum, melanterite, and/or epsomite). None of these phases has been found in association with Martian chloride salt-bearing deposits, leading *Ruesch et al.* [2012] to suggest SO_3-Cl brine fractionation [e.g., *Moore and Bullock*, 1999] as a possible mechanism for forming the Cl-rich brines required for the Martian deposits. This mechanism has been observed in Antarctic permafrosts, resulting in the spatial separation of halide and sulfate deposits [*Dickinson and Rosen*, 2003]. Another possibility is that additional evaporite phases do occur in these regions but are (1) present at low enough abundances (likely less than a few percent) to remain undetected in both VNIR and MIR

data or (2) buried by the chloride salt deposits and undetectable. Recent laboratory work has shown that thick coatings of halite can obscure the spectral signatures of materials underneath at MIR wavelengths [*Berger et al.,* 2015], although this has yet to be verified at VNIR wavelengths.

Although halite is often found in association with other evaporite phases in lacustrine or playa depositional settings [e.g., *Lynch et al.,* 2015, and references therein], its presence as a major phase in these settings is consistent with the inferred abundances for the Martian deposits. Still, the apparent lack of additional evaporite phases, either due to geochemical fractionation or optical masking effects, must be addressed when comparing the Martian deposits to terrestrial lacustrine evaporative environments. This work also shows that ~75–90% of the chloride salt deposits are composed of a silicate component that is spectrally consistent with the local basaltic regolith or, in three cases, the globally homogenous dust. Aeolian input of the silicate material, either through sand saltation or dust suspension and deposition, into a lacustrine/playa environment could explain the substantial silicate fraction. Alternatively, pervasive groundwater upwelling into a porous basaltic regolith could explain the observed spectral and thermophysical features.

5. Conclusions

We have shown that THEMIS observations, supported by TES, CRISM, and OMEGA, of chloride salt-bearing deposits on Mars are consistent with ~10–25% halite mixed with the regional Martian regolith. The spectral character of the chloride-bearing materials displays significant differences that are dependent on the particle size and abundance of the intermixed materials. Where regional coarse particulates are present, THEMIS data show a concave up spectral shape superimposed on a blue spectral slope. Where fine-particulate dust is present, THEMIS spectra of these deposits are characterized by a concave down spectral shape, similar to silicate transmission spectra, superimposed on a blue slope.

We have used spectra of physical mixtures of halite and flood basalt and a hybrid T-matrix/Hapke scattering model to constrain the particle size and abundance of halite in the Martian chloride salt-bearing deposits. When convolved to THEMIS spectral sampling, laboratory and modeled spectra of the coarsest particulates and halite contents $<10\%$ or $>25\%$ fail to match typical THEMIS spectra of these units. Rather, particle sizes between 63 and 180 µm and halite contents between 10 and 25% are consistent with the THEMIS data in regions with coarse particulate surfaces. In the cases with regional fine-particulate materials, particle sizes <10 µm and abundances of 10 to 25% are required to match the THEMIS data. These sites all occur in moderately dusty regions on Mars. This work has also shown that the position of the emissivity maximum in THEMIS spectra of chloride salt-bearing deposits is controlled by the salt abundance, with an emissivity maximum in band 3 (centered near 1270 cm^{-1}; 7.89 µm) indicating a relatively low abundance $< \sim 10\%$ and an emissivity maximum in band 4 (centered near 1170 cm^{-1}; 8.51 µm) indicating higher abundances between 10 and 25%.

The abundances and composition of chloride salt derived in this work help to constrain the formation mechanism(s) of the deposits. Hydrothermal brine deposition or cold brine precipitation is unlikely, as observed chloride salt contents attributed to both of these processes are much too low to explain the observed THEMIS data. A major outstanding question is the apparent lack of other major evaporite phases, including sulfates, phyllosilicates, and carbonates, associated with most of the deposits. The data presented here are most consistent with the presence of halite as a major phase deposited in either a lacustrine/playa setting or in association with late-stage groundwater upwelling.

References

Bandfield, J. L. (2006), Extended surface exposures of granitoid compositions in Syrtis Major, Mars, *Geophys. Res. Lett.*, *33*, L06203, doi:10.1029/2005GL025559.
Bandfield, J. L., V. E. Hamilton, and P. R. Christensen (2000), A global view of Martian surface compositions from MGS-TES, *Science*, *287*(5458), 1626–1630, doi:10.1126/science.287.5458.1626.
Bandfield, J. L., D. Rogers, M. D. Smith, and P. R. Christensen (2004a), Atmospheric correction and surface spectral unit mapping using Thermal Emission Imaging System data, *J. Geophys. Res.*, *109*, E10008, doi:10.1029/2004JE002289.
Bandfield, J. L., V. E. Hamilton, P. R. Christensen, and H. Y. McSween (2004b), Identification of quartzofeldspathic materials on Mars, *J. Geophys. Res.*, *109*, E10009, doi:10.1029/2004JE002290.
Berger, J. A., P. L. King, A. Green, M. A. Craig, M. N. Spilde, S. P. Wright, T. S. Kunkel, and R. J. Lee (2015), Effect of halite coatings on thermal infrared spectra, *J. Geophys. Res. Solid Earth*, *120*, 2162–2178, doi:10.1002/2014JB011712.

Bishop, J. L., R. Quinn, and M. D. Dyar (2014), Spectral and thermal properties of perchlorate salts and implications for Mars, *Am. Mineral.*, *99*, 1580–1592.

Bridges, J. C., and M. M. Grady (1999), A halite-siderite-anhydrite-chlorapatite assemblage in Nakhla: Mineralogical evidence for evaporites on Mars, *Meteorit. Planet. Sci.*, *34*, 407–416.

Bridges, J. C., and M. M. Grady (2000), Evaporite mineral assemblages in the nakhlite (Martian) meteorites, *Earth Planet. Sci. Lett.*, *176*, 267–279.

Carter, J., and F. Poulet (2013), Ancient plutonic processes on Mars inferred from the detection of possible anorthositic terrains, *Nat. Geosci.*, *6*, 1008–1012.

Christensen, P. R., and R. L. Fergason (2013), THEMIS-derived thermal inertia mosaic of Mars: Product description and science results, Abstract 2822 presented at Lunar Planet. Sci. XLIV.

Christensen, P. R., J. L. Bandfield, M. D. Smith, V. E. Hamilton, and R. N. Clark (2000), Identification of a basaltic component on the Martian surface with Thermal Emission Spectrometer data, *J. Geophys. Res.*, *105*, 9609–9621, doi:10.1029/1999JE001127.

Christensen, P. R., et al. (2005), Evidence for magmatic evolution and diversity on Mars from infrared observations, *Nature*, *436*, 504–509.

Christensen, P. R., E. Engle, S. Anwar, S. Dickensheid, D. Noss, N. Gorelick, and M. Weiss-Malik (2009), JMARS-A planetary GIS, Abstract IN22A-06 presented at 2009 AGU Fall Meeting.

Cohen, M. D., R. C. Flagan, and J. H. Seinfel (1987), Studies of concentrated electrolyte solutions using the electrodynamic balance, 1, water activities for single electrolyte solutions, *J. Phys. Chem.*, *91*, 4563–4574.

Cull, S., R. E. Arvidson, J. G. Catalano, D. W. Ming, R. V. Morris, M. T. Mellon, and M. Lemmon (2010), Concentrated perchlorate at the Mars Phoenix landing site: Evidence for thin film liquid water on Mars, *Geophys. Res. Lett.*, *37*, L22203, doi:10.1029/2010GL045269.

Davila, A. F., et al. (2010), Hygroscopic salts and the potential for life on Mars, *Astrobiology*, *10*, 617–628.

Day, P. R. (1965), Particle fractionation and particle-size analysis, in *Methods of Soil Analysis, Part 1: Physical and Mineralogical Properties, Including Statistics of Measurement and Sampling*, edited by C. A. Black et al., pp. 545–567, Am. Soc. of Agron., Inc., Madison, Wis.

Dickinson, W. W., and M. R. Rosen (2003), Antarctic permafrost: An analogue for water and diagenetic minerals on Mars, *Mem. Geol. Soc. Am.*, *3*, 199–202.

Donev, A., S. Torquato, and F. H. Stilinger (2005), Neighbor list collision-driven molecular dynamics simulation for nonspherical hard particles: II. Applications to ellipses and ellipsoids, *J. Comput. Phys.*, *202*, 765–793.

El-Maarry, M. R., A. Pommerol, and N. Thomas (2013), Analysis of polygonal cracking patterns in chloride-bearing terrains on Mars: Indicators of ancient playa settings, *J. Geophys. Res. Planets*, *118*, 2263–2278, doi:10.1002/2013JE004463.

El-Maarry, M. R., W. Watters, N. K. McKewon, J. Carter, E. N. Dobrea, J. L. Bishop, A. Pommerol, and N. Thomas (2014), Potential desiccation cracks on Mars: A synthesis from modeling, analogue-field studies, and global observations, *Icarus*, *241*, 248–268.

Eugster, H. P., and L. A. Hardie (1978), Saline Lakes, in *Lakes: Chemistry, Geology, Physics*, edited by A. Lerman, pp. 237–293, Springer, New York.

Fergason, R. L., P. R. Christensen, and H. H. Kieffer (2006), High resolution thermal inertia derived from the Thermal Emission Imaging System (THEMIS): Thermal model and applications, *J. Geophys. Res.*, *111*, E12004, doi:10.1029/2006JE002735.

Gee, G. W., and J. W. Bauder (1986), Particle-size analysis, in *Methods of Soil Analysis, Part 1: Physical and Mineralogical Methods*, edited by A. Klute, pp. 383–411, Am. Soc. of Agron., Inc., Soil Sci. Soc. of Am., Inc., Madison, Wis.

Gendrin, A., et al. (2005), Sulfates in Martian layered terrains: The OMEGA/Mars Express view, *Science*, *307*, 1587–1591.

Gillespie, A. R., A. B. Kahle, and R. E. Walker (1986), Color enhancement of highly correlated images. 1. Decorrelation and Hsi contrast stretches, *Remote Sens. Environ.*, *20*(3), 209–235, doi:10.1016/0034-4257(86)90044-1.

Glavin, D. P., et al. (2013), Evidence for perchlorates and the origin of chlorinated hydrocarbons detected by SAM at the Rocknest aeolian deposit in Gale crater, *J. Geophys. Res. Planets*, *118*, 1955–1973, doi:10.1002/jgre.20144.

Glotch, T. D., and G. R. Rossman (2009), Mid-infrared reflectance spectra and optical constants of six iron oxide/oxyhydroxide phases, *Icarus*, *204*, 663–671.

Glotch, T. D., G. R. Rossman, and O. Aharonson (2007), Mid-infrared (5-100 μm) reflectance spectra and optical constants of ten phyllosilicate minerals, *Icarus*, *192*, 605–622.

Glotch, T. D., J. L. Bandfield, L. L. Tornabene, H. B. Jensen, and F. P. Seelos (2010), Distribution and formation of chlorides and phyllosilicates in Terra Sirenum, Mars, *Geophys. Res. Lett.*, *37*, L16202, doi:10.1029/2010GL044557.

Gooding, J. L., S. J. Wentworth, and M. E. Zolensky (1991), Aqueous alteration of the Nakhla meteorite, *Meteoritics*, *26*(2), 135–143.

Greenspan, L. (1977), Humidity fixed points of binary saturated aqueous solutions, *J. Res. Natl. Bur. Stand.*, *81A*, 89–96.

Hamilton, V. E., and S. W. Ruff (2012), Distribution and characteristics of Adirondack-class basalt as observed by Mini-TES in Gusev crater, Mars and its possible volcanic source, *Icarus*, *218*, 917–949.

Hapke, B. (1996), A model of radiative and conductive energy transfer in planetary regoliths, *J. Geophys. Res.*, *101*, 16,817–16,831, doi:10.1029/96JE00917.

Hecht, M. H., et al. (2009), Detection of perchlorate and the soluble chemistry of martian soil at the Phoenix Lander Site, *Science*, *325*, 64–67.

Hynek, B. M., M. M. Osterloo, and K. S. Kierein-Young (2015), Late stage formation of Martian chloride salts through ponding and evaporation, Abstract 1045 presented at Lunar Planet. Sci. XLVI.

Jensen, H. B., and T. D. Glotch (2011), Investigation of the near infrared spectral character of putative Martian chloride deposits, *J. Geophys. Res.*, *116*, E00J03, doi:10.1029/2011JE003887.

Kounaves, S. P., et al. (2010), Wet Chemistry experiments on the 2007 Phoenix Mars Scout Lander Mission: Data analysis and results, *J. Geophys. Res.*, *115*, E00E10, doi:10.1029/2009JE003424.

Lynch, K. L., B. H. Horgan, J. Munakata-Marr, J. Hanley, R. Schneider, K. A. Rey, J. R. Spear, W. A. Jackson, and S. M. Ritter (2015), Near-infrared spectroscopy of lacustrine sediments in the Great Salt Lake Desert: An analog study for Martian paleolake basins, *J. Geophys. Res. Planets*, *120*, 599–623, doi:10.1002/2014JE004707.

Mackowski, D. W., and M. I. Mishchenko (1996), Calculation of the T matrix and the scattering matrix for ensembles of spheres, *J. Opt. Soc. Am. A*, *13*, 2266–2278.

Mackowski, D. W., and M. I. Mishchenko (2011), A multiple sphere T-matrix Fortran code for use on parallel computer clusters, *J. Quant. Spectrosc. Radiat. Transfer*, *112*, 2182–2192.

McLennan, S. M., et al. (2005), Provenance and diagenesis of the evaporite-bearing Burns formation, Meridiani Planum, Mars, *Earth Planet. Sci. Lett.*, *240*, 95–121.

Miller, F. A., and C. H. Wilkins (1952), Infrared spectra and characteristic frequencies of inorganic ions, *Anal. Chem.*, *24*, 1253–1294.

Ming, D. W., et al. (2013), Volatile and organic compositions of sedimentary rocks in Yellowknife Bay, Gale Crater, Mars, *Science*, *343*, 1245267.

Mishchenko, M. I. (1994), Asymmetry parameters of the phase function for densely packed scattering grains, *J. Quant. Spectrosc. Radiat. Transfer*, *52*, 95–110.

Moore, J. M., and M. A. Bullock (1999), Experimental studies of Mars-analog brines, *J. Geophys. Res.*, *104*, 21,925–21,939, doi:10.1029/1999JE001040.

Morris, R. V., D. C. Golden, D. W. Ming, T. G. Graff, R. E. Arvidson, S. M. Wiseman, K. A. Lichtenberg, and S. Cull (2009), Visible and near-IR reflectance spectra for smectite, sulfate, and perchlorate under dry conditions for interpretation of Martian surface mineralogy, Abstract 2317 presented at Lunar Planet. Sci. XL.

Murchie, S. L., et al. (2009), A synthesis of Martian aqueous mineralogy after 1 Mars year of observations from the Mars Reconnaissance Orbiter, *J. Geophys. Res.*, *114*, E00D06, doi:10.1029/2009JE003342.

Naughton, J. J., V. A. Lewis, D. Hammond, and D. Nishimoto (1974), The chemistry of sublimates collected directly from lava fountains at Kilauea Volcano, Hawaii, *Geochim. Cosmochim. Acta*, *38*, 1679–1690.

Navarro-Gonzalez, R., E. Vaargas, J. de la Rosa, A. C. Raga, and C. P. McKay (2010), Reanalysis of the Viking results suggests perchlorate and organics at midlatitudes on Mars, *J. Geophys. Res.*, *115*, E12010, doi:10.1029/2010JE003599.

Nesbitt, H. W., and R. E. Wilson (1992), Recent chemical weathering of basalts, *Am. J. Sci.*, *292*, 740–777.

Osterloo, M. M., and B. M. Hynek (2015), Martian chloride deposits: The last gasps of widespread surface water, Abstract 1054 presented at Lunar Planet. Sci. XLVI.

Osterloo, M. M., V. E. Hamilton, J. L. Bandfield, T. D. Glotch, A. M. Baldridge, P. R. Christensen, L. L. Tornabene, and F. S. Anderson (2008), Chloride-bearing materials in the southern highlands of Mars, *Science*, *319*, 1651–1654.

Osterloo, M. M., F. S. Anderson, V. E. Hamilton, and B. M. Hynek (2010), Geologic context of proposed chloride-bearing materials on Mars, *J. Geophys. Res.*, *115*, E10012, doi:10.1029/2010JE003613.

Pejov, L., and V. Petruševski (2002), Fourier transform infrared study of perchlorate ($^{35}ClO_4{}^-$ and $^{37}ClO_4{}^-$) anions isomorphously associated in potassium permanganate matrix. Vibrational anharmonicity and pseudo-symmetry effects, *J. Phys. Chem. Solids*, *63*, 1873–1881.

Presley, M. A., and P. R. Christensen (1997), Thermal conductivity measurements of particulate materials. 2. Results, *J. Geophys. Res.*, *102*(E3), 6551–6566.

Putzig, N. E., and M. T. Mellon (2007), Apparent thermal inertia and the surface heterogeneity of Mars, *Icarus*, *191*, 68–94.

Rivera-Hernandez, F., J. L. Bandfield, S. W. Ruff, and M. J. Wolff (2015), Characterizing the thermal infrared spectral effects of optically thin surface dust: Implications for remote-sensing and in situ measurements of the martian surface, *Icarus*, *262*, 173–186.

Rogers, A. D., and P. R. Christensen (2007), Surface mineralogy of Martian low-albedo regions from MGS-TES data: Implications for upper crustal evolution and surface alteration, *J. Geophys. Res.*, *112*, E01003, doi:10.1029/2006JE002727.

Rogers, A. D., and H. Nekvasil (2015), Feldspathic rocks on Mars: Compositional constraints from infrared spectroscopy and possible formation mechanisms, *Geophys. Res. Lett.*, *42*, 2619–2626, doi:10.1002/2015GL063501.

Ruesch, O., F. Poulet, M. Vincendon, J.-P. Bibring, J. Carter, G. Erkeling, B. Gondet, H. Hiesinger, A. Ody, and D. Reiss (2012), Compositional investigation of the proposed chloride-bearing materials on Mars using near-infrared orbital data from OMEGA/Mex, *J. Geophys. Res.*, *117*, E00J13, doi:10.1029/2012JE004108.

Ruff, S. W., P. R. Christensen, P. W. Barbera, and D. L. Anderson (1997), Quantitative thermal emission spectroscopy of minerals: A laboratory technique for measurement and calibration, *J. Geophys. Res.*, *102*(B7), 14,899–14,913.

Ruff, S. W., and P. R. Christensen (2002), Bright and dark regions on Mars: Particle size and mineralogical characteristics based on Thermal Emission Spectrometer data, *J. Geophys. Res.*, *107*(E12), 5119, doi:10.1029/2001JE001580.

Ruff, S. W., P. R. Christensen, D. L. Blaney, W. H. Farrand, J. R. Johnson, J. R. Michalski, J. E. Moersch, S. P. Wright, and S. W. Squyres (2006), The rocks of Gusev Crater as viewed by the Mini-TES instrument, *J. Geophys. Res.*, *111*, E12S18, doi:10.1029/2006JE002747.

Sagan, C., and J. Pollack (1967), Anisotropic nonconservative scattering and the clouds of Venus, *J. Geophys. Res.*, *72*, 469–477.

Salemi, E., U. Tessari, N. Colombani, and M. Mastrocicco (2010), Improved gravitational grain size separation method, *Appl. Clay Sci.*, *48*(4), 612–614, doi:10.1016/j.clay.2010.03.014.

Sautter, V., et al. (2015), *In situ* evidence for continental crust on early Mars, *Nat. Geosci.*, *8*, 605–609.

Sutter, B., et al. (2016), Oxychlorine Species on Mars, *Int. J. Astrobiol.*, in press.

Schmidt, M. E., et al. (2008), Hydrothermal origin of halogens at Home Plate, Gusev Crater, *J. Geophys. Res.*, *113*, E06S12, doi:10.1029/2007JE003027.

Spitzer, W. G., and D. A. Kleinman (1961), Infrared lattice bands of quartz, *Phys. Rev.*, *121*, 1324–1335.

Taylor, G. J., et al. (2006), Variations in K/Th on Mars, *J. Geophys. Res.*, *111*, E03S06, doi:10.1029/2006JE002676.

Tosca, N. J., and S. M. McLennan (2006), Chemical divides and evaporite assemblages on Mars, *Earth Planet. Sci. Lett.*, *241*, 21–31.

Vaniman, D. T., et al. (2013), Mineralogy of a mudstone at Yellowknife Bay, Gale Crater, Mars, *Science*, *343*, 1243480.

Wedepohl, K. H. (1995), The composition of the continental crust, *Geochim. Cosmochim. Acta*, *59*, 1217–1232.

Wiscombe, W. J., and G. W. Grams (1976), The backscattered fraction in two-stream approximations, *J. Atmos. Sci.*, *33*, 2440–2451.

Wolff, M. J., et al. (2006), Constraints on dust aerosols from the Mars Exploration Rovers using MGS overflights and Mini-TES, *J. Geophys. Res.*, *111*, E12S17, doi:10.1029/2006JE002786.

Wray, J. J., S. L. Murchie, S. W. Squyres, F. P. Seelos, and L. L. Tornabene (2009), Diverse aqueous environments on ancient Mars revealed in the southern highlands, *Geology*, *37*, 1043–1046.

Wray, J. J., S. T. Hansen, J. Dufek, G. A. Swayze, S. L. Murchie, F. P. Seelos, J. R. Skok, R. P. Irwin III, and M. S. Ghiorso (2013), Prolonged magmatic activity on Mars inferred from the detection of felsic rocks, *Nat. Geosci.*, *6*, 1013–1017.

Wright, S. P., P. R. Christensen, and T. G. Sharp (2011), Laboratory thermal emission spectroscopy of shocked basalt from Lonar Crater, India, and implications for Mars orbital and sample data, *J. Geophys. Res.*, *116*, E09006, doi:10.1029/2010JE003785.